



## Facet engineering in Au nanoparticles buried in p-Si photocathodes for enhanced photoelectrochemical CO<sub>2</sub> reduction

Jiaxin Hu <sup>a,1</sup>, Ningbo Fan <sup>a,1</sup>, Cong Chen <sup>a</sup>, Yuquan Wu <sup>a</sup>, Zhihe Wei <sup>b</sup>, Bin Xu <sup>a,\*</sup>, Yang Peng <sup>b,\*</sup>, Mingrong Shen <sup>a,\*</sup>, Ronglei Fan <sup>a,\*</sup>

<sup>a</sup> School of Physical Science and Technology, Jiangsu Key Laboratory of Thin Films, Collaborative Innovation Center of Suzhou Nano Science and Technology, Soochow University, 1 Shizi Street, Suzhou 215006, China

<sup>b</sup> Soochow Institute of Energy and Material Innovations, College of Energy, Key Laboratory of Advanced Carbon Materials and Wearable Energy Technologies of Jiangsu Province, Soochow University, 1 Shizi Street, Suzhou 215006, China



### ARTICLE INFO

#### Keywords:

Photoelectrochemical CO<sub>2</sub> reduction  
Facet engineering  
Au nanoparticles  
Silicon photocathode  
Interfacial contact

### ABSTRACT

Converting CO<sub>2</sub> into carbon-based fuels via the photoelectrochemical (PEC) approach is considered as an one-stone-two-birds strategy for alleviating the greenhouse effect and energy crisis. Here, we report a novel two-step strategy to integrate uniform Au NPs with controllable Au(111)/Au(200) boundaries on p-Si photocathodes for efficient and selective PEC CO<sub>2</sub> conversion to CO. Theoretical calculations suggest that the Au(111)/Au(200) boundaries significantly reduce the energy barrier for forming the \*COOH intermediate during CO<sub>2</sub> reduction. Moreover, we discover that embedding the Au NPs into Si surface can not only further improve the PEC activity and selectivity but also significantly boost the operational stability of Si photocathodes, because of the ameliorated interfacial contact between the Au NPs and Si substrate. Eventually, the optimized Au/p-Si photocathode demonstrates a great CO selectivity of 82.2 % and an impressive operational stability of over one week, which offers critical insights into the design of photocathodes for solar fuel production.

### 1. Introduction

Photoelectrochemical (PEC) CO<sub>2</sub> reduction, as an intriguing strategy to produce storable carbon-based fuels by converting intermittent solar energy at ambient conditions, is of great economic and environmental merits for addressing the energy crisis and global warming [1–3]. To this end, numerous studies have been put into developing efficient and stable photocathodes that can activate inert CO<sub>2</sub> molecules at a low overpotential and selectively produce a targeted product [4–6]. As the prevalent semiconductor and photovoltaic material, silicon (Si) holds great perspective as a photocathode for PEC CO<sub>2</sub> reduction reaction (CRR) due to its relatively narrow band gap with efficient light harvesting, superior optoelectronic property, abundant reserves on earth, and the streamlined large-scale production [1,7–9]. Nonetheless, Si photoelectrodes suffer from intrinsically poor catalytic activity and selectivity towards CRR when used alone, and therefore an additional co-catalyst is required to expedite the surface reaction kinetics.

Metals such as Au, Ag and Zn are capable of promoting CRR toward selective production of CO in aqueous solutions [10,11]. Particularly, Au

is known as a state-of-the-art catalyst for selective CO formation, because it has a CO binding energy closer to the ideal value than any of the other metals [12]. Catalytic performance of the metals can be further enhanced by tuning surface morphology and atomic arrangement, which has been met with some success on catalyzing Si photocathodes [8,13–15]. For instance, Oh et al. have shown that electrochemical pretreatment is effective in controlling the surface morphology of Au thin film, leading to dramatic increase in the activity and selectivity of Si photoelectrodes [8]. Despite the witnessed effectiveness, 200 nm thick Au thin film is the general prerequisite, which unavoidably causes parasitic light consumption and therefore a trade-off between CRR performance and optical harvesting. Hence, it would be of particular interest to shatter the uninterrupted metal film catalysts on Si photocathodes into isolated nanoparticles (NPs). On the other hand, CRR kinetics on metals are strongly influenced by the surface atomic arrangement [16,17]. Both experimental and theoretical researches have revealed that the high-index facets (such as Au(211)) are more active in converting CO<sub>2</sub> into CO than the low-index facets (for example, Au(111)), due to the presence of under-coordinated atoms with

\* Corresponding authors.

E-mail addresses: [binxu19@suda.edu.cn](mailto:binxu19@suda.edu.cn) (B. Xu), [ypeng@suda.edu.cn](mailto:ypeng@suda.edu.cn) (Y. Peng), [mrshen@suda.edu.cn](mailto:mrshen@suda.edu.cn) (M. Shen), [rlfan@suda.edu.cn](mailto:rlfan@suda.edu.cn) (R. Fan).

<sup>1</sup> These authors contributed equally to this work.

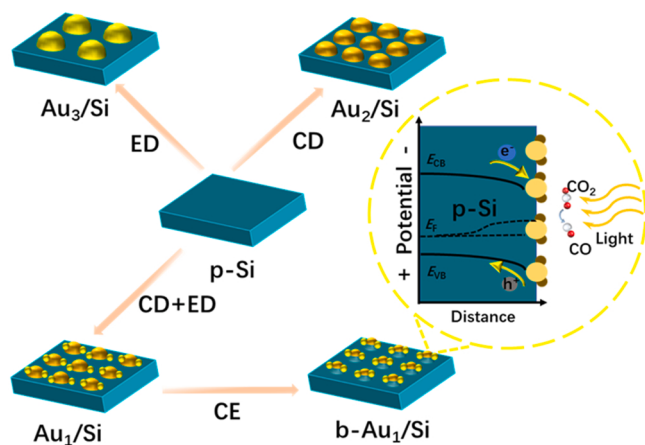


**Fig. 1.** Schematic illustration of the fabrication of Au NPs in varying forms on p-Si photocathodes *via* different protocols.

abundant dangling bonds and high free energy [17–20]. In this vein, Au NPs manifesting high-index facets have been fabricated, usually through wet-chemistry synthesis and colloidal stabilization [21,22]. However, given that the residual organic surfactants on NPs can greatly diminish the catalytic activities, these NPs have some intrinsic limitations when integrated with PEC devices [23]. Therefore, it is highly desired to direct

integrate crystalline Au NPs expressing high-index facets with Si photocathodes, so as to mitigate issues of surface passivation and contamination that are detrimental to the CRR process [24]. Moreover, while extensive efforts have been made to exploit the high-index facets of metal NPs, less attention is paid to the heterojunction of two different facets (A.K.A. grain boundary), although these crystalline boundaries may contribute significantly to the overall CRR activity and selectivity [25,26].

Another major challenge for the PEC system has been the trade-off between photoelectrode stability and efficiency [27–30]. The efficiency of Si photoelectrodes used in aqueous PEC systems normally degrades with surface oxidation, leading to a high kinetic barrier of electron transfer from Si to the surface co-catalyst [31,32]. Consequently, many studies have been devoted to implementing a conformal metal oxide layer to protect the Si surface and passivate the co-catalyst/Si interface [9,28,29,33,34]. However, these co-catalyst/Si interfaces often suffer from weak physical adhesion and poor electronic contact, especially when the co-catalyst layer takes the form of metal NPs in limited contact with the underlying electrode surface. This is probably the primary cause for constrained operational stability of photocathodes observed in literatures of PEC water splitting and CO<sub>2</sub> reduction. New strategies are thus needed to generate better co-catalyst/semiconductor interface for simultaneously promoting the charge transport across the co-catalyst/Si interface and stabilizing metal NPs on the Si surface.

In this study, uniform Au NPs with controllable Au(111)/Au(200)

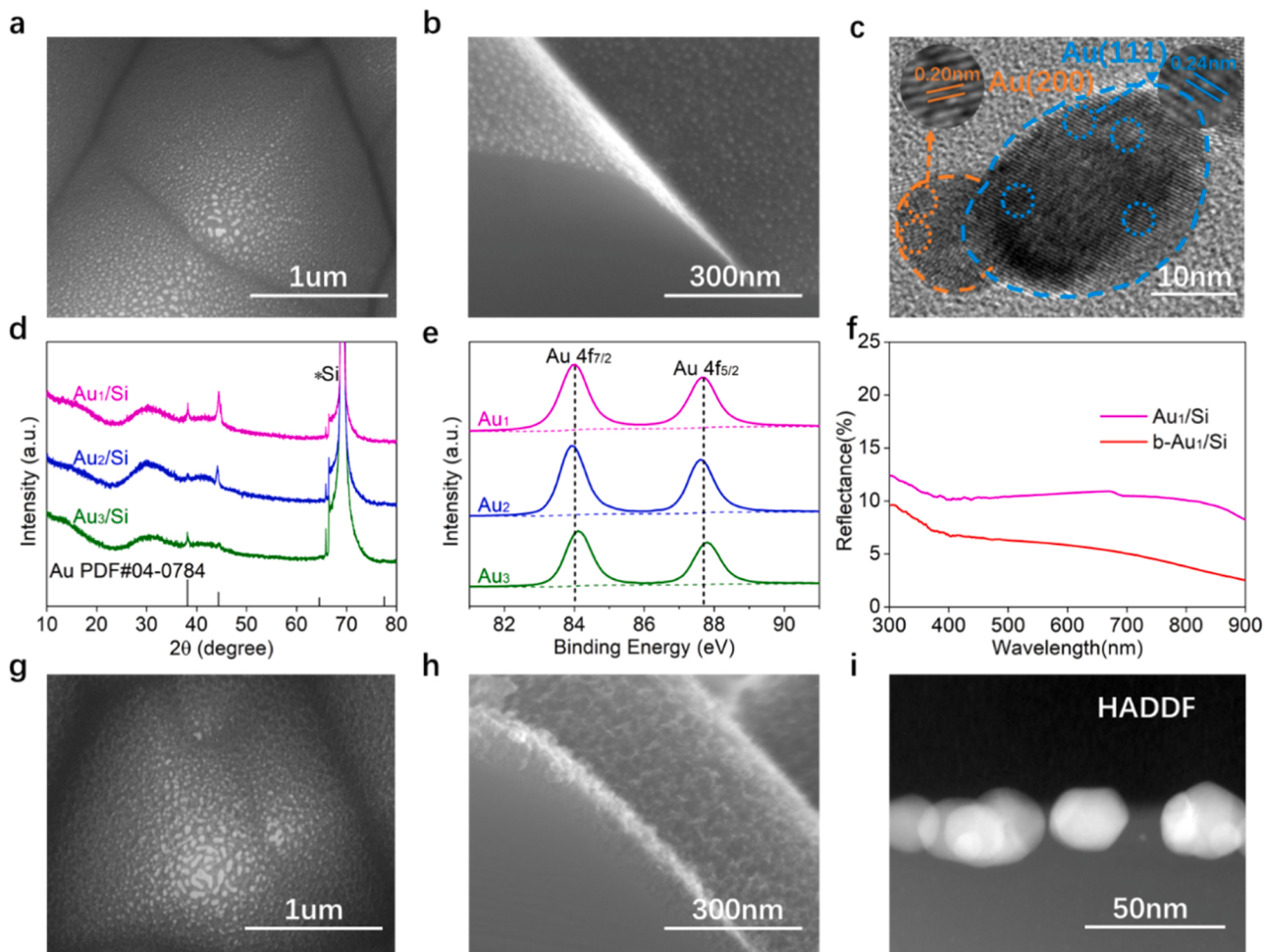


**Fig. 2.** Characterization of the as-prepared Si photocathodes. (a) Top-view, (b) cross-section SEM images and (c) high-resolution TEM image of Au NPs from the Au<sub>1</sub>/Si sample. (d) XRD patterns and (e) high-resolution XPS Au 4f spectra taken on the Au<sub>1</sub>/Si, Au<sub>2</sub>/Si and Au<sub>3</sub>/Si photocathodes. (f) Reflection spectra of the Au<sub>1</sub>/Si and b-Au<sub>1</sub>/Si photocathodes. (g) Top-view, (h) cross-section SEM images and (i) HAADF image of b-Au<sub>1</sub>/Si.

boundaries were successfully deposited on the p-Si surface (named Au<sub>1</sub>/Si) for PEC CO formation through a consecutive chemical- and electro-deposition protocol. Compared with Si photocathodes with similarly sized Au NPs enclosed by the Au(200) facet or Au(111) facet alone (named Au<sub>2</sub>/Si and Au<sub>3</sub>/Si, respectively), the Au<sub>1</sub>/Si photocathode exhibits remarkably activity and selectivity for reduction of CO<sub>2</sub> to CO. Corroborated with density functional theory (DFT) calculations, the enhancement in the CRR performance is attributed to the substantially improved catalytic activity at the Au(111)/Au(200) interfaces, which are energetically favorable for CRR to produce CO. More importantly, we find that an additional etching process that partially buries Au NPs into the Si surface (named b-Au<sub>1</sub>/Si) enables to not only improve the PEC activity and selectivity, but also boost the operational stability. The optimized b-Au<sub>1</sub>/Si photocathode exhibits a large photocurrent density of  $\sim 13.1$  mA/cm<sup>2</sup> at  $\sim 1.0$  V *versus* the reversible hydrogen electrode (RHE), a great CO selectivity of 82.2 % and an impressive operational stability of over one week. These findings offer a new strategy for designing CRR photocathodes with better efficiency, selectivity and stability.

## 2. Results and discussion

The fabrication of Si photocathodes began with the construction of surface micropyramid (MP) structures on the boron-doped p-type single-crystal Si wafers, as demonstrated by our former reports and the process supplied in the Experimental Section (Supporting Information) [35–37]. Fig. 1 schematically depicts the fabrication procedure for various forms of Au NPs on the Si photocathodes. For Au<sub>1</sub>/Si, a two-step approach was initiated to fabricate Au NPs on Si electrodes. In the first step, a chemical deposition (CD) method was implemented to deposit small and uniform Au seeds onto the p-Si surface, taking advantage of the galvanic displacement reaction between Au ions and elemental Si [13]. Afterwards, an electrodeposition (ED) process was conducted to continually grow Au on the above CD Au seeds while maintaining the homogeneous distribution. To investigate the virtue of the photocathode fabricated by this two-step approach, Au NPs were also deposited on p-Si by using CD or ED alone to prepare the control samples, denoted as Au<sub>2</sub>/Si and Au<sub>3</sub>/Si, respectively. The Au contents by various deposition methods on Si photocathodes were all controlled at  $\sim 0.1$  mg cm<sup>-2</sup>, which can be experimentally determined by monitoring the change of Au contents in the Au precursor solution after Au NPs deposition *via* inductively coupled plasma-atomic emission spectrometry (ICP-AES) (Tables S1–S5). To further improve the interfacial contact between the Au NPs and the Si electrode, the Au<sub>1</sub>/Si was subjected to a metal-assisted chemical etching (CE) process in HF solution containing H<sub>2</sub>O<sub>2</sub> for different period [38], resulting in Au NPs partially buried into the Si electrodes, which is denoted as b-Au<sub>1</sub>/Si for simplicity. Fig. 1 also displays the catalytic mechanism of b-Au<sub>1</sub>/Si photocathode. Under illumination, the incident photons are absorbed by the p-Si semiconductor, generating electron–hole pairs in Si. The photogenerated electrons in Si separate and transport to the electrolyte/electrode interface near the Au NPs, where PEC CRR takes place.

SEM images of Au<sub>2</sub>/Si and Au<sub>3</sub>/Si with different size and distribution of Au NPs synthesized by the one-step CD or ED protocol are first provided in Fig. S1–2. With the ED process alone, Au NPs with the average sizes of 30, 40 and 60 nm was observed on Si surface. Interestingly, Au NPs deposited through the CD process were found to be more dispersed, making possible the fine control of distribution and morphology of Au NPs on Au<sub>1</sub>/Si. Unless otherwise stated, Au<sub>1</sub>/Si hereafter refers to the sample with a CD-Au/ED-Au ratio of 1.88, since this photocathode shows the best PEC performance. Fig. 2a–b demonstrates the top-view and cross-section scanning electron microscopy (SEM) images of the Au<sub>1</sub>/Si sample. In contrast to the smooth surface of bare p-Si (Fig. S3), Au NPs with an average size of  $\sim 20$  nm are formed homogeneously on the Si surface (Fig. S4). The morphology and crystalline features of Au NPs, stripped off from the surface of Au<sub>1</sub>/Si photocathode by

ultrasonication, were also investigated *via* transmission electron microscope (TEM). High-resolution TEM images in Fig. 2c and Fig. S5 revealed lattice fringes with d-spacings of 0.20 and 0.24 nm, corresponding to the (200) and (111) lattice planes of FCC Au, respectively.

The crystalline structure of the as-prepared samples was characterized by X-ray diffraction (XRD) (Fig. 2d). Apart from the characteristic peak of the Si substrate located at 69.1°, two diffraction peaks at 2θ = 38.2° and 44.4°, ascribed to the Au (111) and (200) planes (JCPDS Card No. 04–0784), respectively, were observed on all samples of Au<sub>1</sub>/Si, Au<sub>2</sub>/Si and Au<sub>3</sub>/Si with varying intensity ratios. On Au<sub>3</sub>/Si, Au(111) dominates the lattice of Au NPs. In our cases, an ultra-low cathodic current density of  $\sim 0.1$  mA/cm<sup>2</sup> was applied during the electrodeposition process, thus causing the kinetically favored growth of the Au (111) facet, possibly due to the low surface free energy of (111) facet than that of other facets [39]. On the other hand, the dictating plane on Au<sub>2</sub>/Si is Au(200), suggesting that Au NPs formed through the CD process are apt to grow along the (200) crystal orientation. During the CD process, Au ions near the Si surface capture electrons from Si and deposit on the Si surface in the form of metallic Au nuclei, while the Si around the Au nuclei is oxidized to SiO<sub>2</sub>, which is the replacement reaction [40]. A large potential difference of 2.62 V between the Au<sup>3+</sup>/Au and SiF<sub>6</sub><sup>2-</sup>/Si redox couples could provide potential driving force to deposit Au NPs with high surface free energy of Au(200) facet [41,42]. As expected, the Au<sub>1</sub>/Si sample synthesized in two steps displays both prominent peaks of Au(111) and Au(200), which echo the TEM observation. These results suggest that different synthetic protocol results in different crystalline orientation and the two-step synthesized Au NPs on Au<sub>1</sub>/Si encompass enormous (200)/(111) facets and junctions.

To further examine the electronic properties of Au NPs on different samples, X-ray photoelectron spectroscopy (XPS) was implemented (Fig. 2e). For the Au<sub>3</sub>/Si sample, two peaks at binding energies (BE) of 87.8 and 84.1 eV are ascribed to the metallic Au<sup>0</sup> 4 f<sub>5/2</sub> and Au<sup>0</sup> 4 f<sub>7/2</sub> [35]. Compared to Au<sub>3</sub>/Si, a slight shift of  $\sim 0.1$  eV to lower BE was observed for Au<sub>2</sub>/Si. Such shift of BE indicates that the Au<sub>2</sub>/Si expressing majorly Au(200) planes contains a higher electron density in the Au valence orbitals than that of Au<sub>3</sub>/Si exposing mainly Au(111), which should help to mediate the adsorption of reaction intermediates in PEC CRR [43,44]. More importantly, the BE of Au 4 f for Au<sub>1</sub>/Si is located between those of Au<sub>3</sub>/Si and Au<sub>2</sub>/Si, further attesting the formation of Au NPs with mixed crystalline phases and junctions on the surface of the Si photocathode.

After being subject to the etching process, the as-obtained photocathode of b-Au<sub>1</sub>/Si turned into black with a significantly reduced surface reflection (Fig. S6), which is quantitatively confirmed by the reflectance spectra. As shown in Fig. 2f, in comparison to Au<sub>1</sub>/Si, the etched photocathode of b-Au<sub>1</sub>/Si exhibits a drop of light reflectance to below 10 % in the full range of visible light from 300 to 900 nm. The optical reflectance results agree well with those of the UV-vis absorption spectra (Fig. S7). We surmise that this phenomenon is mainly due to the generation of a gradient nanoporous surface layer, which is witnessed by SEM images shown in Fig. 2g and h. Different from the Au<sub>1</sub>/Si sample exhibiting only Au NPs that are affixed to the Si surface, b-Au<sub>1</sub>/Si displays many Au NPs partially buried into the Si surface, which can be further demonstrated by energy dispersive X-ray (EDX) mapping images shown in Fig. S8. To probe the surface structure of b-Au<sub>1</sub>/Si in more details, a cross-sectional TEM analysis was conducted. Fig. 2i shows the high-angle annular dark field (HAADF) image of b-Au<sub>1</sub>/Si, confirming that Au NPs are partially embedded into the Si substrate. This helps to furnish an intimate contact between the Au NPs and Si substrate, which is beneficial for photoexcited charge transfer.

All the PEC experiments were carried out in a custom-built two-compartment cell separated by an anion conduction membrane filled with CO<sub>2</sub>-saturated 0.1 M KHCO<sub>3</sub> under simulated AM 1.5 G one sun illumination (Fig. S9). The size and distribution of Au NPs on the PEC LSV curves and potential-dependent FE<sub>s</sub> for CO and H<sub>2</sub> of the Au<sub>2</sub>/Si and Au<sub>3</sub>/Si samples were provided in Figs. S10 and S11. The mass ratio of

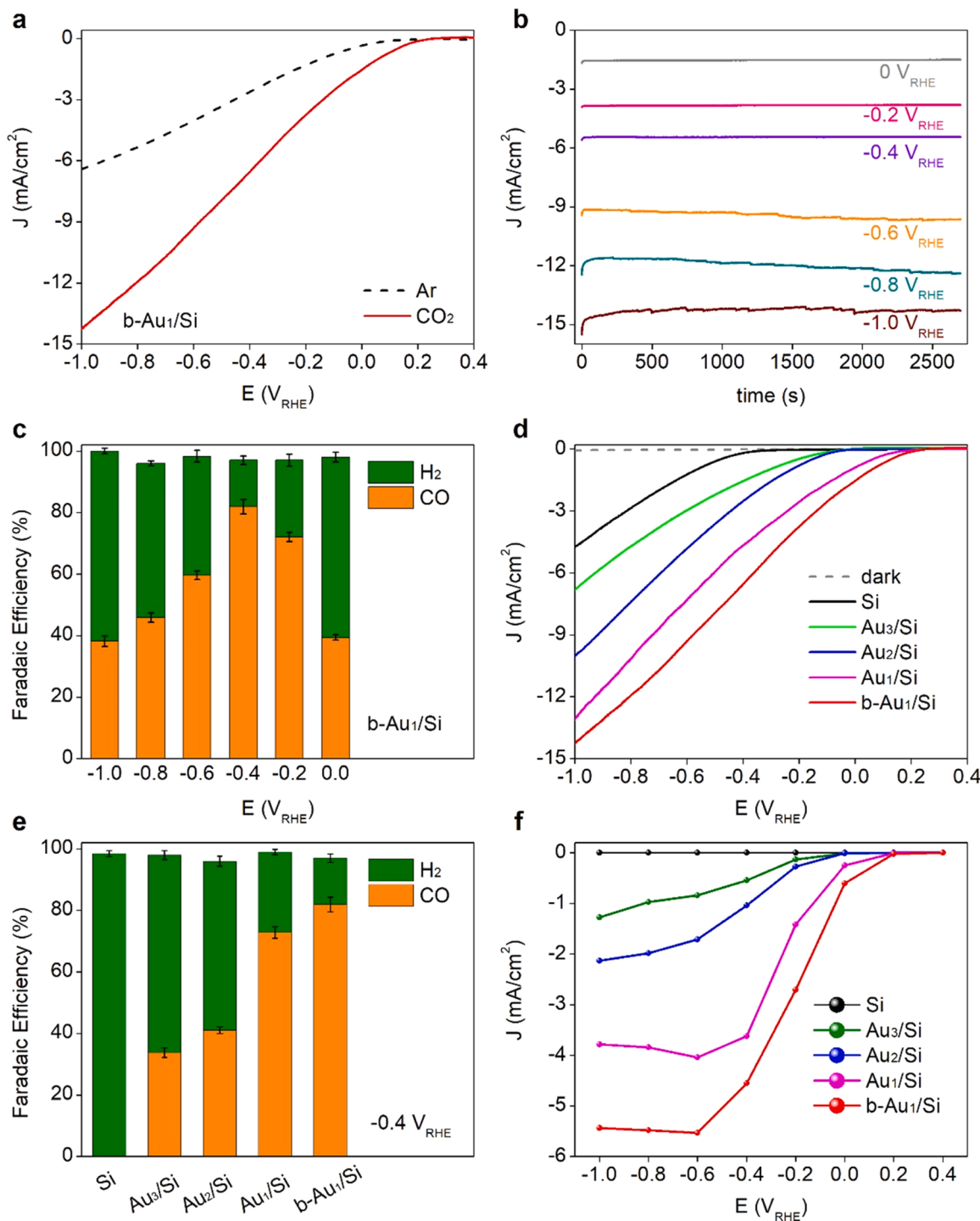


**Fig. 3.** PEC CRR performances. (a) LSV curves recorded in  $\text{N}_2$ -saturated and  $\text{CO}_2$ -saturated  $0.1 \text{ M KHCO}_3$ , (b) potentiostatic  $i$ - $t$  curves of CRR at varying bias and (c) potential-dependent FEs of  $\text{CO}$  and  $\text{H}_2$  for the  $\text{b-Au}_1/\text{Si}$  photocathode. (d) LSV curves, (e) FEs of  $\text{CO}$  at  $-0.4 \text{ V}_{\text{RHE}}$  and (f) partial current density of  $\text{CO}$  for all investigated Si photocathodes.

CD-Au to ED-Au on  $\text{Au}_1/\text{Si}$  and the subsequent etching time were also optimized for  $\text{b-Au}_1/\text{Si}$  with the results given in Fig. S12 and S13. The PEC CRR properties of the  $\text{b-Au}_1/\text{Si}$  photocathode were first explored by linear sweep voltammetry (LSV) in  $0.1 \text{ M KHCO}_3$  purged with Ar or  $\text{CO}_2$ . As shown in Fig. 3a, in the  $\text{CO}_2$ -purged electrolyte  $\text{b-Au}_1/\text{Si}$  exhibited a strong enhancement in both photocurrent and onset potential ( $V_{\text{on}}$ , defined as the potential at  $-0.1 \text{ mA}/\text{cm}^2$ ), and such enhancement is much more remarkable than that manifested by the control samples including  $\text{Au}_1/\text{Si}$ ,  $\text{Au}_2/\text{Si}$  and  $\text{Au}_3/\text{Si}$  (Fig. S14). The significantly

enhanced photocurrent and  $V_{\text{on}}$  on  $\text{b-Au}_1/\text{Si}$  in the  $\text{CO}_2$ -saturated electrolyte attest to its superb PEC CRR activity [45].

To detect the CRR products on  $\text{b-Au}_1/\text{Si}$ , chronoamperometric measurements were conducted at varying applied potentials (Fig. 3b). Stable current densities were measured during the PEC CRR at all potentials, and the values increased with the decreasing potentials. The produced gaseous products were periodically sampled by an on-line gas chromatography (GC), detecting  $\text{CO}$  and  $\text{H}_2$  as the reaction products. In accordance with nuclear magnetic resonance (NMR) results, we also

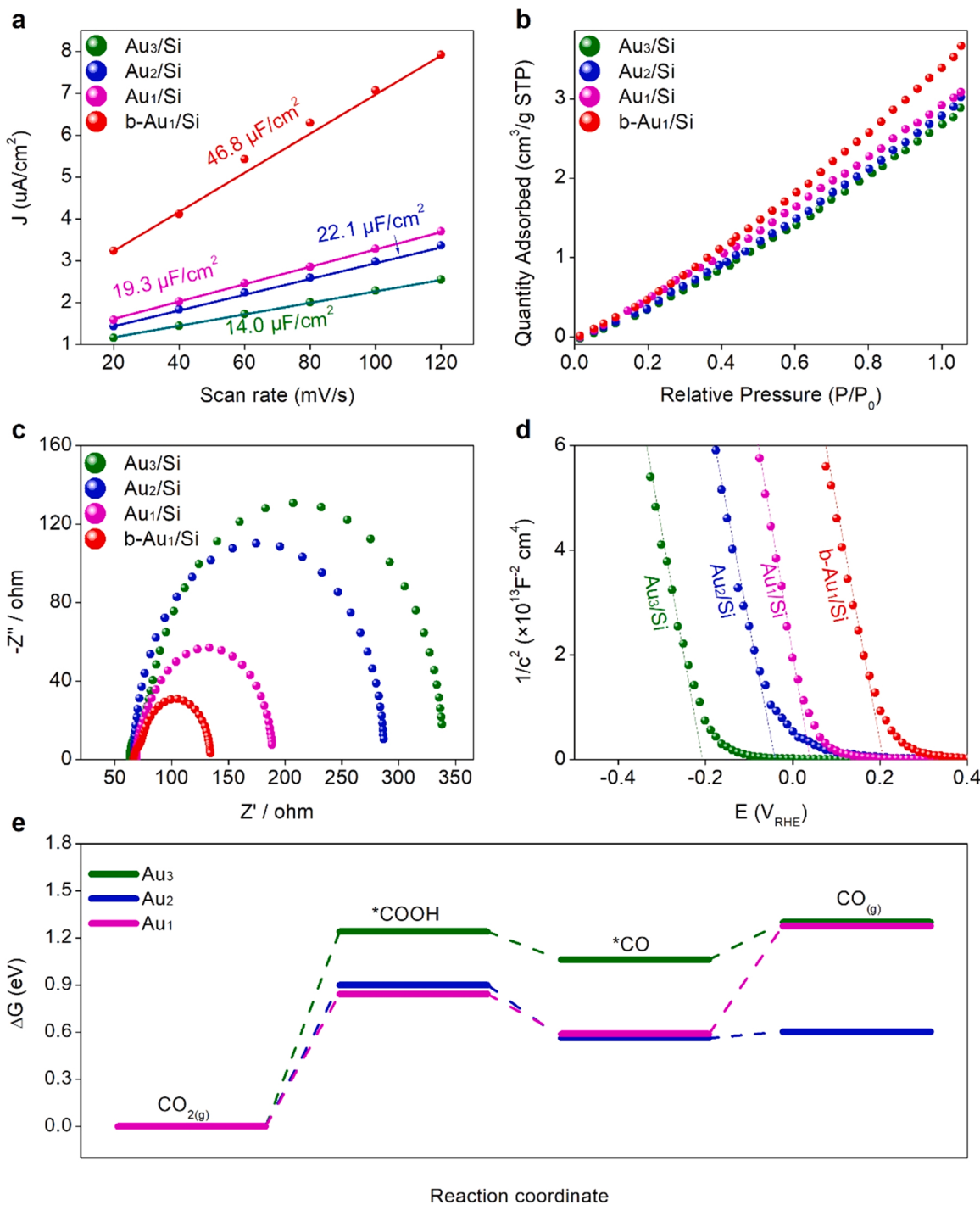


**Fig. 4.** PEC analyses on the charge transfer kinetics and CRR mechanism. (a) current density plots at various scan rates, (b) CO<sub>2</sub> adsorption-desorption isotherms, (c) EIS spectra and (d) Mott-Schottky plots of various Si photocathodes. (e) DFT calculated free energy diagrams for CO<sub>2</sub> reduction to CO on the Au(111), Au(200) surfaces and the Au(111)/Au(200) junction.

found that no liquid products (such as HCOOH and CH<sub>3</sub>OH) were discovered in the electrolyte, indicating the almost 100 % FE of CO + H<sub>2</sub> in our devices (Fig. S15). Using high-purity <sup>13</sup>CO<sub>2</sub> as the feeding gas we confirmed that the CO product was solely originated from CO<sub>2</sub>, rather than the organic sealing used (Fig. S16). Fig. 3c plots the FEs of CO and H<sub>2</sub> as a function of the applied potential for b-Au<sub>1</sub>/Si. The FE of CO on b-Au<sub>1</sub>/Si increases with the decreasing potential until reaching a maximum value of 82.2 % at -0.4 V<sub>RHE</sub>. Beyond that, the decrease in FE for CO could be attributed to: 1) competitive hydrogen evolution reaction (HER) [46], and 2) CO<sub>2</sub> transport limit. That is, the rapid

consumption of CO<sub>2</sub> on the surface of Si photocathode at lower applied potentials cannot be effectively compensated due to its low solubility and slow diffusion in H-cell [47].

To gain insights into the high performance of b-Au<sub>1</sub>/Si, PEC measurements were also conducted on the Au<sub>1</sub>/Si, Au<sub>2</sub>/Si and Au<sub>3</sub>/Si control samples (Fig. 3d). In the absence of light, the bare p-Si photocathodes generated negligible cathodic current. Upon illumination, the bare p-Si shows a negative V<sub>on</sub> of -0.35 V<sub>RHE</sub> and a photocurrent of -4.7 mA/cm<sup>2</sup> at -1.0 V<sub>RHE</sub> (j-1.0 V). Integration of Au NPs onto the Si photocathode by either ED or CD route can effectively promote the

photocurrent and  $V_{on}$  in the order of  $\text{Au}_3/\text{Si} < \text{Au}_2/\text{Si}$ , which are further improved on  $\text{Au}_1/\text{Si}$  ( $V_{on} = 0.13 \text{ V}_{\text{RHE}}$ ,  $j_{1.0 \text{ V}} = -11.0 \text{ mA/cm}^2$ ) with the co-existence of  $\text{Au}(200)$  and  $\text{Au}(111)$  facets and junctions. These observations suggest that the polycrystallinity and grain boundaries lent a better catalytic activity to  $\text{Au}_1/\text{Si}$ , when compared to monolithic  $\text{Au}_2/\text{Si}$  and  $\text{Au}_3/\text{Si}$  samples. More remarkably, embedding Au NPs into the Si electrode enables to further raise the performance bar of the b- $\text{Au}_1/\text{Si}$  photocathode, achieving a photocurrent density of  $-13.1 \text{ mA/cm}^2$  at  $-1.0 \text{ V}_{\text{RHE}}$  and a more positive  $V_{on}$  of  $0.22 \text{ V}_{\text{RHE}}$ , thanks to the ameliorated interfacial contact between the Au NPs and Si substrate. To explore the roles of light field and electric field in  $\text{CO}_2$  reduction, we further conduct the experiments on the photocatalytic and electrocatalytic activity of the b- $\text{Au}_1/\text{Si}$  photocathode. When the light field is applied along, b- $\text{Au}_1/\text{Si}$  produces nearly zero photocurrent (Fig. S17). This is reasonable because the band structure of p-Si based photocathode can't provide enough driving force to generate photocurrent in this situation [7]. On the other hand, in the absence of light, b- $\text{Au}_1/\text{Si}$  can only produce a small current of  $-1 \text{ mA/cm}^2$  at  $-1.0 \text{ V}_{\text{RHE}}$ , and a maximum CO FE of 6.5 % is obtained at  $-1.0 \text{ V}_{\text{RHE}}$  (Fig. S18). The strongest photocurrent and CO FE of b- $\text{Au}_1/\text{Si}$  under PEC condition demonstrate that both light field and electric field are indispensable for improving the activity and selectivity of CO generation. Fig. 3e compares the FEs of CO on different Si photocathodes at  $-0.4 \text{ V}_{\text{RHE}}$ . It was not absurd to see that the bare p-Si showed negligible FE of CO formation, while the product selectivity of CO increased to 33.3 % and 40.1 % on monolithic  $\text{Au}_3/\text{Si}$  and  $\text{Au}_2/\text{Si}$ , respectively. Strikingly, the FE of CO increased drastically to 73.2 % on  $\text{Au}_1/\text{Si}$  containing both  $\text{Au}(200)$  and  $\text{Au}(111)$  facets and the junctions in between. By further embedding Au NPs into the Si substrate a superb CO FE of 82.2 % can be achieved, ranking among the best of Si photocathodes reported in literature for PEC CRR under the light intensity of  $100 \text{ mW cm}^{-2}$  (Table S6). The critical role of surface atomic arrangement of Au and interfacial contact between the Au NPs and Si in selective CO production was further confirmed by comparing the CO FEs at other potentials ranging from  $-1.0 \text{ V}_{\text{RHE}}$  (Fig. S19). The CO yield rates of all tested Si photocathodes were compared through partial current densities as shown in Fig. 3f. Just as expected, b- $\text{Au}_1/\text{Si}$  achieved the highest CO partial current density within the whole potential range, followed consequently by  $\text{Au}_1/\text{Si}$ ,  $\text{Au}_2/\text{Si}$ ,  $\text{Au}_3/\text{Si}$  and p-Si. Note that a high CO partial current density of  $-4.1 \text{ mA/cm}^2$  was achieved at  $-0.4 \text{ V}_{\text{RHE}}$ , which was impressive and superior to most of the previously reported Si photocathodes (Table S6). Thus, we conclude that both the conversion rate and selectivity of  $\text{CO}_2$  to CO can be synergistically boosted by the biphasic Au crystalline structure and the intimate Au/Si interface on b- $\text{Au}_1/\text{Si}$ .

To pursue the mechanistic understanding of the superior PEC performance of the b- $\text{Au}_1/\text{Si}$  photocathode, comprehensive PEC analyses were carried out. Electrochemically active surface areas (ECSAs) were first studied by measuring the double-layer capacitance (Fig. S20). As shown in Fig. 4a, the measured  $C_{dl}$  value of  $\text{Au}_1/\text{Si}$  is  $22.1 \mu\text{F cm}^{-2}$ , larger than that of  $\text{Au}_2/\text{Si}$  ( $19.3 \mu\text{F cm}^{-2}$ ) and  $\text{Au}_3/\text{Si}$  ( $14.0 \mu\text{F cm}^{-2}$ ), suggesting that the biphasic Au NPs comprising  $\text{Au}(200)/\text{Au}(111)$  facets and junctions possess higher specific surface area than their monolithic counterparts. After the etching process, the obtained b- $\text{Au}_1/\text{Si}$  exhibited an even higher  $C_{dl}$  of  $46.8 \mu\text{F cm}^{-2}$ , likely due to the formation of nanostructured surface on the Si electrode. This unique electrode architecture consequently endows b- $\text{Au}_1/\text{Si}$  with increased  $\text{CO}_2$  adsorption capacity, as evidenced by the  $\text{CO}_2$  adsorption isotherms shown in Fig. 4b. Specifically, the amount of adsorbed  $\text{CO}_2$  over b- $\text{Au}_1/\text{Si}$  at 1 atm ( $3.38 \text{ cm}^3 \text{ g}^{-1}$ ) is 1.16, 1.22 and 1.27 times higher than that on  $\text{Au}_1/\text{Si}$  ( $2.91 \text{ cm}^3 \text{ g}^{-1}$ ),  $\text{Au}_2/\text{Si}$  ( $2.78 \text{ cm}^3 \text{ g}^{-1}$ ) and  $\text{Au}_3/\text{Si}$  ( $2.67 \text{ cm}^3 \text{ g}^{-1}$ ). Given the fact that  $\text{CO}_2$  adsorption is the prerequisite for CRR in aqueous media [48], the enhanced  $\text{CO}_2$  adsorption capacity of b- $\text{Au}_1/\text{Si}$  helps to overcome the mass transport limit.

Electrochemical impedance spectroscopy (EIS) characterizations were further carried out to examine the charge transfer behaviors in various Si photocathodes. Fig. 4c shows the EIS spectra recorded at

$-0.4 \text{ V}_{\text{RHE}}$  in the  $\text{CO}_2$ -saturated  $0.1 \text{ M KHCO}_3$ , fitted using the equivalent circuit exhibited in Fig. S21.  $\text{Au}_1/\text{Si}$  showed a smaller charge transfer resistance ( $R_{ct}$ ) of  $117.4 \Omega$  when compared to those of  $\text{Au}_2/\text{Si}$  ( $218.3 \Omega$ ) and  $\text{Au}_3/\text{Si}$  ( $265.5 \Omega$ ), corroborating that the integration of biphasic Au NPs with rich grain boundaries onto the Si surface helps to promote the charge transfer kinetics. The charge transfer resistance can be further decreased to  $64.2 \Omega$  after embedding Au NPs into the Si electrode, attesting to the further enhanced charge transfer on account of the intimate interfacial contact between the Au NPs and Si surface. The enhanced charge transfer of b- $\text{Au}_1/\text{Si}$  was also confirmed by the photocurrent transient measurements, which were performed at the potential of  $-0.4 \text{ V}_{\text{RHE}}$  during repeated on/off illumination periods (Fig. S22). As expected, the b- $\text{Au}_1/\text{Si}$  exhibits a weakest spike transient photocurrent when the light is switched on/off, suggesting the excellent interface quality with the lowest recombination rate of the electron-hole pairs among other control samples [49,50].

It has been reported that the  $V_{on}$  in photocathodes are positively correlated with the flat-band potential ( $V_{FB}$ ) of semiconductor materials [35,51]. Hence, the positive  $V_{on}$  shift of b- $\text{Au}_1/\text{Si}$  photocathode was examined by the Mott–Schottky analysis, where the  $V_{FB}$  can be calculated by deducing the linear portion of the curve from Mott–Schottky plots [38]. The b- $\text{Au}_1/\text{Si}$  sample showed a more positive  $V_{FB}$  of  $0.21 \text{ V}_{\text{RHE}}$  in comparison with  $\text{Au}_1/\text{Si}$  ( $0.05 \text{ V}_{\text{RHE}}$ ),  $\text{Au}_2/\text{Si}$  ( $-0.04 \text{ V}_{\text{RHE}}$ ), and  $\text{Au}_3/\text{Si}$  ( $-0.21 \text{ V}_{\text{RHE}}$ ), consistent with their  $V_{on}$  values reflected in LSV curves, respectively (Fig. 4d). This higher  $V_{FB}$  of  $\text{Au}_1/\text{Si}$  indicating a higher band bending in the depletion region, which can be attributed to the lower work function of Au NPs on  $\text{Au}_1/\text{Si}$  relative to those on the  $\text{Au}_2/\text{Si}$  and  $\text{Au}_3/\text{Si}$  as determined by the ultraviolet photoelectron spectroscopy (UPS; Fig. S23) [43,52]. Furthermore, the subsequent etching of  $\text{Au}_1/\text{Si}$  lends a further increase in  $V_{FB}$  by  $0.16 \text{ V}$ , suggesting that the interfacial charge recombination between the Au NPs and Si surface can be suppressed by ameliorating the interfacial contact.

To understand the dependence of CRR activity on the surface atomic arrangement of Au, DFT calculations were performed on the modelled  $\text{Au}(111)/\text{Au}(200)$  junction, comprising a pyramidal  $\text{Au}(111)$  cluster on top of the planar  $\text{Au}(200)$  plane (Fig. S24). The results were compared to those obtained from  $\text{Au}(111)$  and  $\text{Au}(200)$  surfaces alone (Figs. S25 and S26). It has been well reckoned that the reduction path of  $\text{CO}_2$  to CO involves the following elementary steps:  $\text{CO}_2 \rightarrow *_{\text{COOH}} \rightarrow *_{\text{CO}} \rightarrow \text{CO(g)}$ , and the highest free energy barrier from the rate-determining step can be used for a good activity descriptor [47,53]. Fig. 4e displays the free energy diagrams along the reaction coordinates with the corresponding intermediate configurations illustrated in Fig. S24–26. In all cases, the initial  $\text{CO}_2$  hydrogenation for  $*_{\text{COOH}}$  formation constitutes the rate-determining step, which is in agreement with previous results on Au-based catalysts [47,54]. On the biphasic  $\text{Au}(111)/\text{Au}(200)$  structure, the free-energy barrier of the rate-determining step is  $0.84 \text{ eV}$ , being lower than those on the standalone  $\text{Au}(111)$  ( $1.24 \text{ eV}$ ) and  $\text{Au}(200)$  ( $0.90 \text{ eV}$ ) facets. Therefore, the CRR process is more efficiently catalyzed at the  $\text{Au}(111)/\text{Au}(200)$  junction, which reasonably explains the superior CO production on  $\text{Au}_1/\text{Si}$  in comparison to  $\text{Au}_2/\text{Si}$  and  $\text{Au}_3/\text{Si}$ .

Operational stability is also an important criterion in constructing photoelectrodes for practical applications. The long-term stability of the  $\text{Au}_1/\text{Si}$  and b- $\text{Au}_1/\text{Si}$  photocathodes was measured in  $\text{CO}_2$ -saturated  $0.1 \text{ M KHCO}_3$  at  $-0.4 \text{ V}_{\text{RHE}}$  under simulated AM 1.5 G one sun illumination. To retain the same experimental conditions throughout the stability test, the electrolyte was refreshed every 8 h since in the overall reaction the production of CO is at the expense of protons. For the  $\text{Au}_1/\text{Si}$  sample, already 50 % of the initial photocurrent density was lost by the end of 30 h testing, together with the drop of CO FE from 71.9 % to 20.1 % (Fig. S27). The loss of CO activity and selectivity after the prolonged operation can be ascribed to the stripping of Au NPs from the Si photocathode, as clearly witnessed by SEM images taken on the post-electrolytic photocathode (Fig. S28). In sharp contrast, the b- $\text{Au}_1/\text{Si}$  photocathode enables to maintain a stabilized current density of

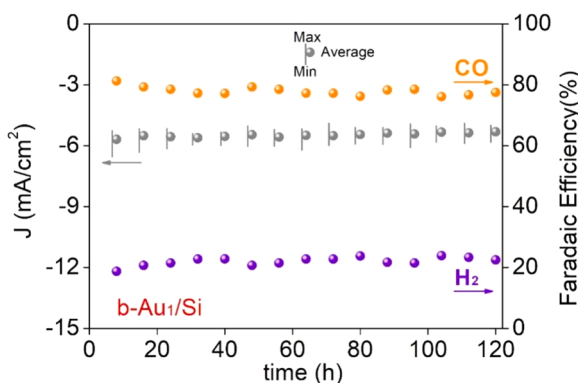


**Fig. 5.** Chronoamperometric PEC CRR stability of the b-Au<sub>1</sub>/Si photocathode tested at  $-0.4\text{ V}_{\text{RHE}}$ .

$-5.3\text{ mA/cm}^2$  for up to 120 h, with the FE of CO continuously exceeding 76.1 % (Fig. 5). The PEC LSV curves and potential-dependent FEs for CO and H<sub>2</sub> are also well preserved after stability test, indicating the superior stability of b-Au<sub>1</sub>/Si photocathode again (Fig. S29). To the best of our knowledge, such a high stability of PEC CRR outperforms all that previously reported for Si-based photocathodes (with the longest being 20 h, Table S6). In addition, the structural durability of b-Au<sub>1</sub>/Si after 120 h of prolonged testing was further confirmed by SEM, XRD, XPS and optical characterizations. SEM images showed that on b-Au<sub>1</sub>/Si both the Si surface texture and coverage of Au NPs were unchanged (Fig. S30). XRD and XPS measurements revealed virtually identical crystalline features and electronic properties of Au NPs when compared to their pristine states (Fig. S31). UV-vis reflection and absorption spectra suggested the light absorption characteristics of b-Au<sub>1</sub>/Si were well maintained after 120 h of testing (Fig. S32). These analyses provide compelling evidences for the superb stability of b-Au<sub>1</sub>/Si in driving PEC CRR, in virtue of the robust biphasic configuration of Au NPs and intimate contact at the Au/Si interface.

### 3. Conclusion

To sum up, this work developed an innovative two-step approach to fabricate well dispersed Au NPs with controllable Au(111)/Au(200) boundaries onto the p-Si photocathode for converting CO<sub>2</sub> to CO. This resulting Au<sub>1</sub>/Si photocathode demonstrated remarkable PEC activity and selectivity for CO production, compared to the Si photocathodes with similarly sized Au NPs enclosed by Au(200) facet or Au(111) facet alone. Such enhancement in PEC properties originate from the substantially catalytic active sites at the Au(111)/Au(200) boundaries that are energetically favorable for CRR to CO, as revealed by experiments and DFT calculations. Moreover, by further embedding the Au NPs into Si surface, our b-Au<sub>1</sub>/Si photocathode exhibits not only improved PEC activity and selectivity for CO formation, but also a great promotion in operational stability, which can be attributed to the robust contact at Au/Si interface. Eventually, the optimized Si photocathode achieves a photocurrent density of  $-13.1\text{ mA/cm}^2$  at  $-1.0\text{ V}_{\text{RHE}}$ , a Faradaic efficiency of 82.2 % and an operational stability of over one week for CO formation. The facet engineering in this work provides new strategies for the fabrication of more efficient selective and stable photocathodes for solar-driven fuel production.

### CRediT authorship contribution statement

**Jiaxin Hu:** Conceptualization, Methodology, Formal analysis, Investigation, Data Curation, Writing - Original draft. **Ningbo Fan:** Software, Investigation, Formal analysis. **Cong Chen:** Conceptualization, Methodology, Investigation, Data Curation, Writing - Original draft. **Yuquan Wu:** Validation, Formal analysis, Investigation. **Zhihe**

**Wei:** Formal analysis, Investigation. **Bin Xu:** Software, Investigation, Writing - Review & Editing. **Yang Peng:** Formal analysis, Investigation, Writing - Review & Editing, Supervision. **Mingrong Shen:** Writing - Review & Editing, Supervision, Project administration, Funding acquisition. **Ronglei Fan:** Conceptualization, Formal analysis, Investigation, Data Curation, Writing - Original draft, Writing - Review & Editing, Supervision, Project administration, Funding acquisition.

### Declaration of Competing Interest

The authors declare that they have no known competing financial interests or personal relationships that could have appeared to influence the work reported in this paper.

### Data Availability

Data will be made available on request.

### Acknowledgements

This work was supported by National Natural Science Foundation of China (Grant No. 52002259 and 51672183), and a key project of carbon peak carbon neutralization technology support from Suzhou Science and Technology Bureau (Grant No. ST202227).

### Appendix A. Supporting information

Supplementary data associated with this article can be found in the online version at doi:10.1016/j.apcatb.2023.122438.

### References

- [1] X.X. Chang, T. Wang, P.P. Yang, G. Zhang, J.L. Gong, The development of cocatalysts for photoelectrochemical CO<sub>2</sub> reduction, *Adv. Mater.* 31 (2019) 1804710, <https://doi.org/10.1002/adma.201804710>.
- [2] B.W. Zhou, X.H. Kong, S. Vanka, S.B. Cheng, N. Pant, S. Chu, P. Ghamari, Y. C. Wang, G. Botton, H. Cuo, Z.T. Mi, A GaN:Sn nanoarchitecture integrated on a silicon platform for converting CO<sub>2</sub> to HCOOH by photoelectrocatalysis, *Energy Environ. Sci.* 12 (2019) 2842–2848, <https://doi.org/10.1039/c9ee01339c>.
- [3] A.M. Bahamponur, M. Signorile, O. Krocher, Recent progress in syngas production via catalytic CO<sub>2</sub> hydrogenation reaction, *Appl. Catal. B-Environ.* 295 (2021), 120319, <https://doi.org/10.1016/j.apcatb.2021.120319>.
- [4] X. Chang, T. Wang, J. Gong, CO<sub>2</sub> photo-reduction: insights into CO<sub>2</sub> activation and reaction on surfaces of photocatalysts, *Energy Environ. Sci.* 9 (2016) 2177–2196, <https://doi.org/10.1039/c6ee00383d>.
- [5] P. Ding, T. Jiang, N. Han, Y. Li, Photocathode engineering for efficient photoelectrochemical CO<sub>2</sub> reduction, *MT Nano* 10 (2020), 100077, <https://doi.org/10.1016/j.mtnano.2020.100077>.
- [6] S. Chu, P.F. Ou, P. Ghamari, S. Vanka, B.W. Zhou, I. Shih, J. Song, Z.T. Mi, Photoelectrochemical CO<sub>2</sub> Reduction into Syngas with the Metal/Oxide Interface, *J. Am. Chem. Soc.* 140 (2018) 7869–7877, <https://doi.org/10.1021/jacs.8b03067>.
- [7] K. Sun, S.H. Shen, Y.Q. Liang, P.E. Burrows, S.S. Mao, D.L. Wang, Enabling silicon for solar-fuel production, *Chem. Rev.* 114 (2014) 8662–8719, <https://doi.org/10.1021/cr300459q>.
- [8] J.T. Song, H. Ryoo, M. Cho, J. Kim, J.G. Kim, S.Y. Chung, J. Oh, Nanoporous Au thin films on Si photoelectrodes for selective and efficient photoelectrochemical CO<sub>2</sub> reduction, *Adv. Energy Mater.* 7 (2017) 1601103, <https://doi.org/10.1002/aenm.201601103>.
- [9] J.Y. Zheng, H.J. Zhou, Y.Q. Zou, R.L. Wang, Y.H. Lyu, S.P. Jiang, S.Y. Wang, Efficiency and stability of narrow-gap semiconductor-based photoelectrodes, *Energy Environ. Sci.* 12 (2019) 2345–2374, <https://doi.org/10.1039/c9ee00524b>.
- [10] D.D. Zhu, J.L. Liu, S.Z. Qiao, Recent advances in inorganic heterogeneous electrocatalysts for reduction of carbon dioxide, *Adv. Mater.* 28 (2016) 3423–3452, <https://doi.org/10.1002/adma.201504766>.
- [11] J.L. Qiao, Y.Y. Liu, F. Hong, J.J. Zhang, A review of catalysts for the electroreduction of carbon dioxide to produce low-carbon fuels, *Chem. Soc. Rev.* 43 (2014) 631–675, <https://doi.org/10.1039/c3cs60323g>.
- [12] K.P. Kuhl, T. Hatsuksade, E.R. Cave, D.N. Abram, J. Kibsgaard, T.F. Jarillo-Herrero, Electrocatalytic conversion of carbon dioxide to methane and methanol on transition metal surfaces, *J. Am. Chem. Soc.* 136 (2014) 14107–14113, <https://doi.org/10.1021/ja505791r>.
- [13] Y. Hu, F. Chen, P. Ding, H. Yang, J. Chen, C. Zha, Y. Li, Designing effective Si/Ag interface via controlled chemical etching for photoelectrochemical CO<sub>2</sub> reduction, *J. Mater. Chem. A* 6 (2018) 21906–21912, <https://doi.org/10.1039/c8ta05420g>.
- [14] L.F. Wei, J.C. Lin, S.J. Xie, W.C. Ma, Q.H. Zhang, Z.B. Shen, Y. Wang, Photoelectrocatalytic reduction of CO<sub>2</sub> to syngas over Ag nanoparticle modified p-

Si nanowire arrays, *Nanoscale* 11 (2019) 12530–12536, <https://doi.org/10.1039/c9nr02786f>.

[15] Q. Kong, D. Kim, C. Liu, Y. Yu, Y.D. Su, Y.F. Li, P.D. Yang, Directed assembly of nanoparticle catalysts on nanowire photoelectrodes for photoelectrochemical CO<sub>2</sub> reduction, *Nano Lett.* 16 (2016) 5675–5680, <https://doi.org/10.1021/acs.nanolett.6b02321>.

[16] N. Todoroki, H. Tei, H. Tsurumaki, T. Miyakawa, T. Inoue, T. Wadayama, Surface atomic arrangement dependence of electrochemical CO<sub>2</sub> reduction on gold: online electrochemical mass spectrometric study on low-index Au(hkl) surfaces, *ACS Catal.* 9 (2019) 1383–1388, <https://doi.org/10.1021/acscatal.8b04852>.

[17] M. Liu, Y.J. Pang, B. Zhang, P. De Luna, O. Voznyy, J.X. Xu, X.L. Zheng, C.T. Dinh, F.J. Fan, C.H. Cao, F.P.G. de Arquer, T.S. Safaei, A. Mepham, A. Klinkova, E. Kumacheva, T. Filleteer, D. Sinton, S.O. Kelley, E.H. Sargent, Enhanced electrocatalytic CO<sub>2</sub> reduction via field-induced reagent concentration, *Nature* 537 (2016) 382–386, <https://doi.org/10.1038/nature19060>.

[18] S. Mezzavilla, S. Horsch, I.E.L. Stephens, B. Seger, I. Chorkendorff, Structure sensitivity in the electrocatalytic reduction of CO<sub>2</sub> with gold, *Catal., Angew. Chem. Int. Ed.* 58 (2019) 3774–3778, <https://doi.org/10.1002/anie.201811422>.

[19] J. Herranz, J. Durst, E. Fabbri, A. Patru, X. Cheng, A.A. Permyakova, T.J. Schmidt, Interfacial effects on the catalysis of the hydrogen evolution, oxygen evolution and CO<sub>2</sub>-reduction reactions for (co-)electrolyzer development, *Nano Energy* 29 (2016) 4–28, <https://doi.org/10.1016/j.nanoen.2016.01.027>.

[20] A. Rendon-Calle, Q.H. Low, S.H.L. Hong, S. Builes, B.S. Yeo, F. Calle-Vallejo, How symmetry factors cause potential- and facet-dependent pathway shifts during CO<sub>2</sub> reduction to CH<sub>4</sub> on Cu electrodes, *Appl. Catal. B-Environ.* 285 (2021), 119776, <https://doi.org/10.1016/j.apcatb.2020.119776>.

[21] C.L. Xie, Z.Q. Niu, D. Kim, M.F. Li, P.D. Yang, Surface and interface control in nanoparticle catalysis, *Chem. Rev.* 120 (2020) 1184–1249, <https://doi.org/10.1021/acs.chemrev.9b00220>.

[22] Z.W. Quan, Y.X. Wang, J.Y. Fang, High-index faceted noble metal nanocrystals, *Acc. Chem. Res.* 46 (2013) 191–202, <https://doi.org/10.1021/ar200293n>.

[23] W.L. Zhu, R. Michalsky, O. Metin, H.F. Lv, S.J. Guo, C.J. Wright, X.L. Sun, A. A. Peterson, S.H. Sun, Monodisperse Au nanoparticles for selective electrocatalytic reduction of CO<sub>2</sub> to CO, *J. Am. Chem. Soc.* 135 (2013) 16833–16836, <https://doi.org/10.1021/ja409445p>.

[24] W.J. Dong, I.A. Navid, Y.X. Xiao, J.W. Lim, J.L. Lee, Z.T. Mi, CuS-decorated GaN nanowires on silicon photocathodes for converting CO<sub>2</sub> mixture gas to HCOOH, *J. Am. Chem. Soc.* 143 (2021) 10099–10107, <https://doi.org/10.1021/jacs.1c02139>.

[25] X.J. She, X.W. Zhu, J.M. Yang, Y.H. Song, Y.B. She, D.B. Liu, J.J. Wu, Q. Yu, H. M. Li, Z. Liu, P.M. Ajayan, H. Xu, Grain-boundary surface terminations incorporating oxygen vacancies for selectively boosting CO<sub>2</sub> photoreduction activity, *Nano Energy* 84 (2021), 105869, <https://doi.org/10.1016/j.nanoen.2021.105869>.

[26] H.B. Yu, J.H. Huang, L.B. Jiang, L.J. Leng, K.X. Yi, W. Zhang, C.Y. Zhang, X. Z. Yuan, In situ construction of Sn-doped structurally compatible heterojunction with enhanced interfacial electric field for photocatalytic pollutants removal and CO<sub>2</sub> reduction, *Appl. Catal. B-Environ.* 298 (2021), 120618, <https://doi.org/10.1016/j.apcatb.2021.120618>.

[27] M.G. Walter, E.L. Warren, J.R. McKone, S.W. Boettcher, Q. Mi, E.A. Santori, N. S. Lewis, Solar water splitting cells, *Chem. Rev.* 110 (2010) 6446–6473, <https://doi.org/10.1021/cr1002326>.

[28] N.Y. Labrador, X.X. Li, Y.K. Liu, H.Y. Tan, R.Y. Wang, J.T. Koberstein, T.P. Moffat, D.V. Esposito, Enhanced performance of Si MIS photocathodes containing oxide coated nanoparticle electrocatalysts, *Nano Lett.* 16 (2016) 6452–6459, <https://doi.org/10.1021/acs.nanolett.6b02909>.

[29] J.Y. Zheng, Y.H. Lyu, R.L. Wang, C. Xie, H.J. Zhou, S.P. Jiang, S.Y. Wang, Crystalline TiO<sub>2</sub> protective layer with graded oxygen defects for efficient and stable silicon-based photocathode, *Nat. Commun.* 9 (2018) 3572, <https://doi.org/10.1038/s41467-018-05580-z>.

[30] C. Chen, Y.J. Wang, C.M. Nie, J.X. Shen, Z.H. Wei, S. Zou, X.D. Su, R.L. Fan, Y. Peng, M.R. Shen, Gradient-structuring manipulation in Ni<sub>3</sub>S<sub>2</sub> layer boosts solar hydrogen production of Si photocathode in alkaline media, *Adv. Energy Mater.* 12 (2022) 2102865, <https://doi.org/10.1002/aenm.202102865>.

[31] M. Morita, T. Ohmi, E. Hasegawa, M. Kawakami, M. Ohwada, Growth of native oxide on a silicon surface, *J. Appl. Phys.* 68 (1990) 1272–1281, <https://doi.org/10.1063/1.347181>.

[32] M.J. Kenney, M. Gong, Y.G. Li, J.Z. Wu, J. Feng, M. Lanza, H.J. Dai, High-performance silicon photoanodes passivated with ultrathin nickel films for water oxidation, *Science* 342 (2013) 836–840, <https://doi.org/10.1126/science.1241327>.

[33] R.L. Fan, W. Dong, L. Fang, F.G. Zheng, M.R. Shen, More than 10 % efficiency and one-week stability of Si photocathodes for water splitting by manipulating the loading of the Pt catalyst and TiO<sub>2</sub> protective layer, *J. Mater. Chem. A* 5 (2017) 18744–18751, <https://doi.org/10.1039/c7ta04986b>.

[34] M.G. Kast, L.J. Enman, N.J. Gurnon, A. Nadarajah, S.W. Boettcher, Solution-deposited F:SnO<sub>2</sub>/TiO<sub>2</sub> as a base-stable protective layer and antireflective coating for microtextured buried-junction H<sub>2</sub>-evolving Si photocathodes, *ACS Appl. Mater. Interfaces* 6 (2014) 22830–22837, <https://doi.org/10.1021/am506999p>.

[35] K. Wang, N.B. Fan, B. Xu, Z.H. Wei, C. Chen, H. Xie, W.X. Ye, Y. Peng, M.R. Shen, R. L. Fan, Steering the pathway of plasmon-enhanced photoelectrochemical CO<sub>2</sub> reduction by bridging Si and Au nanoparticles through a TiO<sub>2</sub> interlayer, *Small* 18 (2022) 2201882, <https://doi.org/10.1002/smll.202201882>.

[36] W. Xun, Y.J. Wang, R.L. Fan, Q.Q. Mu, S. Ju, Y. Peng, M.R. Shen, Activating the MoS<sub>2</sub> basal plane toward enhanced solar hydrogen generation via in situ photoelectrochemical control, *ACS Energy Lett.* 6 (2021) 267–276, <https://doi.org/10.1021/acsenergylett.0c02320>.

[37] J.X. Shen, R.L. Fan, Y.J. Wang, J. Zhou, C. Chen, Z.H. Wei, S. Ju, T. Qian, Y. Peng, M.R. Shen, Oxygen-vacancy-rich nickel hydroxide nanosheet: a multifunctional layer between Ir and Si toward enhanced solar hydrogen production in alkaline media, *Energy Environ. Sci.* 15 (2022) 3051–3061, <https://doi.org/10.1039/d2ee00951j>.

[38] Y. Zhao, N.C. Anderson, K. Zhu, J.A. Aguiar, J.A. Seabold, J. van de Lagemaat, H. M. Branz, N.R. Neale, J. Oh, Oxidatively stable nanoporous silicon photocathodes with enhanced onset voltage for photoelectrochemical proton reduction, *Nano Lett.* 15 (2015) 2517–2525, <https://doi.org/10.1021/acs.nanolett.5b00086>.

[39] X.J. Yi, G. Yu, F.F. Chang, Z.H. Xie, T.N. Tran, B.N. Hu, C.J. Zhong, Electrochemically controlled growth of Au-Pt alloy nanowires and nanodendrites, *Chem. Asian J.* 9 (2014) 2612–2620, <https://doi.org/10.1002/asia.201402442>.

[40] H. Miyake, S. Ye, M. Osawa, Electroless deposition of gold thin films on silicon for surface-enhanced infrared spectroelectrochemistry, *Electrochim. Commun.* 4 (2002) 973–977, [https://doi.org/10.1016/s1388-2481\(02\)00510-6](https://doi.org/10.1016/s1388-2481(02)00510-6).

[41] B. Fabre, L. Hennous, S. Ababou-Girard, C. Meriadec, Electroless patterned assembly of metal nanoparticles on hydrogen-terminated silicon surfaces for applications in photoelectrocatalysis, *ACS Appl. Mater. Interfaces* 5 (2013) 338–343, <https://doi.org/10.1021/am302226q>.

[42] CRC Handbook of Chemistry and Physics, 87th ed.; Taylor and Francis Group: Boca Raton, FL. (2007).<https://doi.org/10.1021/ja069813z>

[43] A.R. Woldu, Y.J. Wang, L.J. Guo, S. Hussain, A.H. Shah, X.H. Zhang, T. He, Ar-plasma activated Au film with under-coordinated facet for enhanced and sustainable CO<sub>2</sub> reduction to CO, *J. CO<sub>2</sub> Util.* 54 (2021), 101776, <https://doi.org/10.1016/j.jcou.2021.101776>.

[44] L. Zhang, F.X. Mao, L.R. Zheng, H.F. Wang, X.H. Yang, H.G. Yang, Tuning metal catalyst with Metal-C3N4 interaction for efficient CO<sub>2</sub> electroreduction, *ACS Catal.* 8 (2018) 11035–11041, <https://doi.org/10.1021/acscatal.8b03789>.

[45] S.K. Choi, U. Kang, S. Lee, D.J. Ham, S.M. Ji, H. Park, Sn-coupled p-Si nanowire arrays for solar formate production from CO<sub>2</sub>, *Adv. Energy Mater.* 4 (2014) 20130164, <https://doi.org/10.1002/aenm.20130164>.

[46] M. Kan, Z.F.W. Yan, X.T. Wang, J.L. Hitt, L.Q. Xiao, J.M. McNeill, Y. Wang, Y. X. Zhao, T.E. Mallouk, 2-aminobenzethiol-functionalized silver-decorated nanoporous silicon photoelectrodes for selective CO<sub>2</sub> reduction, *Angew. Chem. Int. Ed.* 59 (2020) 11462–11469, <https://doi.org/10.1002/anie.202001953>.

[47] D.R. Yang, L. Liu, Q. Zhang, Y. Shi, Y. Zhou, C.G. Liu, F.B. Wang, X.H. Xia, Importance of Au nanostructures in CO<sub>2</sub> electrochemical reduction reaction, *Sci. Bull.* 65 (2020) 796–802, <https://doi.org/10.1016/j.scib.2020.01.015>.

[48] R. Kortlever, J. Shen, K.J.P. Schouten, F. Calle-Vallejo, M.T.M. Koper, Catalysts and reaction pathways for the electrochemical reduction of carbon dioxide, *J. Phys. Chem. Lett.* 6 (2015) 4073–4082, <https://doi.org/10.1021/acs.jpcllett.5b01559>.

[49] P.F. Cheng, Y.W. Liu, M. Ziegler, M. Klingenhof, D. Wang, Z. Zhang, P. Strasser, P. Schaaf, Improving Silicon Photocathode Performance for Water Reduction through Dual Interface Engineering and Integrating ReS<sub>2</sub> Photocatalyst, *ACS Appl. Energ. Mater.*, 8222–8231.<https://doi.org/10.1021/acsaem.2c00761>.

[50] W.T. Hong, Q. Cai, R.C. Ban, X. He, C.Y. Jian, J. Li, J. Li, W. Liu, High-performance silicon photoanode enhanced by gold nanoparticles for efficient water oxidation, *ACS Appl. Mater. Interfaces* 10 (2018) 6262–6268, <https://doi.org/10.1021/acsmi.7b16749>.

[51] C.K. Ku, P.H. Wu, C.C. Chung, C.C. Chen, K. Tsai, H.M. Chen, Y.C. Chang, C. H. Chuang, C.Y. Wei, C.Y. Wen, T.Y. Lin, H.L. Chen, Y.S. Wang, Z.Y. Lee, U. R. Chang, C.W. Luo, D.Y. Wang, B.J. Hwang, C.W. Chen, Creation of 3D textured grapheme/Si Schottky junction photocathode for enhanced photo-electrochemical efficiency and stability, *Adv. Energy Mater.* 9 (2019) 1901022, <https://doi.org/10.1002/aenm.201901022>.

[52] J. Xiao, M.R. Gao, S.B. Liu, J.L. Luo, Hexagonal Zn nanoplates enclosed by Zn(100) and Zn(002) facets for highly selective CO<sub>2</sub> electroreduction to CO, *ACS Appl. Mater. Interfaces* 12 (2020) 31431–31438, <https://doi.org/10.1021/acsmi.0c06891>.

[53] F.H. Li, Q. Tang, Understanding the role of functional groups of thiolate ligands in electrochemical CO<sub>2</sub> reduction over Au(111) from first-principles, *J. Mater. Chem. A* 7 (2019) 19872–19880, <https://doi.org/10.1039/c9ta06851a>.

[54] D.F. Gao, Y. Zhang, Z.W. Zhou, F. Cai, X.F. Zhao, W.G. Huang, Y.S. Li, J.F. Zhu, P. Liu, F. Yang, G.X. Wang, X.H. Bao, Enhancing CO<sub>2</sub> electroreduction with the metal-oxide interface, *J. Am. Chem. Soc.* 139 (2017) 5652–5655, <https://doi.org/10.1021/jacs.7b00102>.